Imaging surface spots from space-borne photometry

A. F. Lanza

INAF-Osservatorio Astrofisico di Catania
Via S. Sofia, 78 - 95123 Catania, Italy
E-mail: `nuccio.lanza@oact.inaf.it`

Abstract. A general introduction to the foundations of spot modelling is given. It considers geometric models of the surface brightness distribution in late-type stars as can be derived from their wide-band optical light curves. Spot modelling is becoming more and more important thanks to the high-precision, high duty-cycle photometric time series made available by space-borne telescopes designed to search for planets through the method of transits. I review approaches based on a few spots as well as more sophisticated techniques that assume a continuous distributions of active regions and adopt regularization methods developed to solve ill-posed problems. The use of transit light curves to map spots occulted by a planet as it moves across the disc of its host star is also briefly described. In all the cases, the main emphasis is on the basic principles of the modelling techniques and on their testing rather than on the results obtained from their application.

1 Introduction

The photosphere of the Sun is not homogeneous. Dark features, called sunspots, appear and evolve during most of the time, while bright faculae are often observed in proximity to sunspots when they are close to the limb. Those structures are due to the interaction of convection with localized magnetic fields. The total sunspot area does not exceed $0.2 - 0.3$ percent of the solar surface. The total facular area can be about one order of magnitude larger, but faculae have a very low contrast close to the disc centre and may not be easily detected there (e.g., Chapman et al. 2001, 2011). Looking at the photosphere with a resolution of the order of $10^2 - 10^3$ km, we see other brightness inhomogeneities associated with magnetic flux tubes that are localized around the borders of the convective cells. In particular, the flux tubes observed around supergranules are brighter than the unperturbed photosphere and form the photospheric network that is best detected on high-resolution magnetograms.

In distant late-type stars, we observe similar photospheric features because those stars have surface convection and magnetic fields produced by a large-scale dynamo, at least if they rotate sufficiently fast (e.g., Berdyugina 2005; Strassmeier 2009; Kővári & Oláh 2014). However, the lack of spatial resolution means that we can detect them only indirectly. During this school several methods to reach this goal have been introduced. Here I focus on the information that can

be extracted from wide-band photometry, especially from the large datasets recently made available by space-borne telescopes designed to look for planetary transits such as CoRoT and Kepler (e.g., Auvergne et al. 2009; Borucki et al. 2010). The typical accuracy of the measured flux is of the order of 20 parts per million (ppm) on a $V = 12$ magnitude G-type star in one hour of integration time, considering that Kepler has a telescope diameter of 95 cm.

The rotation of a star changes the projected area of its surface brightness inhomogeneities leading to a rotational modulation of its optical flux. Moreover, the intrinsic evolution of these inhomogeneities contributes to the flux variations. In principle, it is possible to measure the rotation period from the light modulation provided that the inhomogeneities evolve on a timescale long in comparison with the rotation period. If they evolve on a shorter timescale, the light variations will provide information on their typical lifetime, but they cannot be used as tracers to measure the stellar rotation period. This is the case of the Sun. The time variation of its total irradiance is dominated by active regions produced by magnetic fields. When the modulation is dominated by faculae with a typical lifetime of $50 - 80$ days, i.e., $2 - 3$ rotations, we can apply time-series analysis techniques to measure the rotation period. On the other hand, when sunspots with a lifetime of only $10 - 15$ days dominate, the measurement of the rotation period becomes difficult and imprecise (cf. Lanza et al. 2004).

Several techniques were introduced to analyze time series of stellar optical photometry to derive the rotation period, the longitudes where surface inhomogeneities preferentially form, and their evolution timescales as well as the long-term variations associated with stellar activity cycles, i.e., the phenomena analogous to the eleven-year sunspot cycle (e.g., Jetsu 1996; Donahue et al. 1997a,b; Kolláth & Oláh 2009; Lehtinen et al. 2011; Lindborg et al. 2013; McQuillan et al. 2013; Reinhold et al. 2013; McQuillan et al. 2014). We shall not discuss those techniques here, but shall focus on the foundations of the modelling of the rotational modulation by means of a simple geometrical approach (*spot modelling*). In the case of close eclipsing binaries, we can also exploit the occultation of one component star by the other to scan its disc (*eclipse mapping*, e.g., Collier Cameron 1997; Lanza et al. 1998). This approach becomes particularly powerful when a planet transits across the disc of its parent star. Thanks to its small size in comparison to the stellar disc, a detailed scanning of the occulted band becomes possible (*transit mapping*, e.g., Schneider 2000; Silva 2003). The foundations of such a technique will be also briefly reviewed.

2   Spot modelling with discrete spots

2.1   Model geometry

For the sake of simplicity, let us consider a single, spherical star rotating with a uniform angular velocity $\mathbf{\Omega}$. We assume a Cartesian reference frame fixed in the inertial space (i.e., a non-rotating frame) with the origin O at the barycentre of the star, the z axis along the stellar spin axis ($\hat{z} \equiv \hat{\mathbf{\Omega}}$), and the x and y axes in

the equatorial plane; the x axis is chosen so that the direction pointing towards the observer $\hat{\mathbf{s}} \equiv \hat{OE}$ is contained in the xz plane (see Fig. 1).

Let us consider a point $P(x, y, z)$ on the surface of the star. If we denote its colatitude and its longitude with θ and ϕ, respectively, the Cartesian components of the unit vector $\hat{OP}$ are: $\hat{OP} = (\sin\theta\cos\phi, \sin\theta\sin\phi, \cos\theta)$. Note that ϕ is a linear function of the time t because the star is rotating with an angular velocity Ω. If the longitude of P at the time t_0 is ϕ_0, we have: $\phi(t) = \phi_0 + \Omega(t - t_0)$. The Cartesian components of the unit vector pointing towards the observer are: $\hat{\mathbf{s}} = (\sin i, 0, \cos i)$, where i is the inclination of the stellar spin axis to the line of sight.

The normal $\hat{\mathbf{n}}$ to the stellar surface at the point P is parallel to $\hat{OP}$ because the star is spherical, that is $\hat{\mathbf{n}} = \hat{OP}$. Therefore, the angle ψ between the normal at P and the direction towards the observer is given by the scalar product $\cos\psi = \hat{\mathbf{n}} \cdot \hat{\mathbf{s}} = \hat{OP} \cdot \hat{\mathbf{s}}$. Introducing $\mu \equiv \cos\psi$ and substituting the above expressions for $\hat{OP}$ and $\hat{\mathbf{s}}$ into this relationship, we finally obtain:

$$\mu = \sin i \sin\theta \cos[\phi_0 + \Omega(t - t_0)] + \cos i \cos\theta. \tag{1}$$

2.2 Flux variation produced by an active region

Let us assume a quadratic limb-darkening law for the unperturbed photosphere in the passband of the observations (cf. Gray 2008):

$$I_{\mathrm{u}}(\mu) = I_0(a + b\mu + c\mu^2), \tag{2}$$

where I_{u} is the specific intensity in the given passband; I_0 the intensity at the centre of the disc; a, b, and c the limb-darkening coefficients that verify $a+b+c = 1$. The flux emerging from the stellar disc of radius R is:

$$F_{\mathrm{u}} = 2\pi R^2 \int_0^{\pi/2} I_{\mathrm{u}}(\cos\psi) \cos\psi \sin\psi \, d\psi = 2\pi R^2 \int_0^1 I_{\mathrm{u}}(\mu)\mu \, d\mu, \tag{3}$$

where $dA = 2\pi R^2 \sin\theta d\theta$ is the area of the elementary band on the sphere between colatitudes θ and $\theta + d\theta$, and the factor $\cos\psi$ gives its projection on the plane normal to the line of sight. Substituting the limb-darkening law and performing the integration, we find the unperturbed stellar flux:

$$F_{\mathrm{u}} = \pi R^2 I_0 \left(a + \frac{2}{3}b + \frac{1}{2}c \right). \tag{4}$$

In the Sun and sun-like stars, the photospheric active regions are much smaller than the area of the disc. Therefore, we can simplify our treatment by considering point-like active regions. Each one consists of a spotted area A_{s} and a facular area A_{f} localized at the same point P with $A_{\mathrm{s}}, A_{\mathrm{f}} \ll \pi R^2$ (cf. Lanza et al. 2003). The flux perturbation produced by that active region, i.e., by its dark spots and bright faculae localized in P, is:

$$\Delta F = \Delta F_{\mathrm{s}} + \Delta F_{\mathrm{f}} = A_{\mathrm{s}}\mu(I_{\mathrm{s}} - I_{\mathrm{u}}) + A_{\mathrm{f}}\mu(I_{\mathrm{f}} - I_{\mathrm{u}}), \tag{5}$$
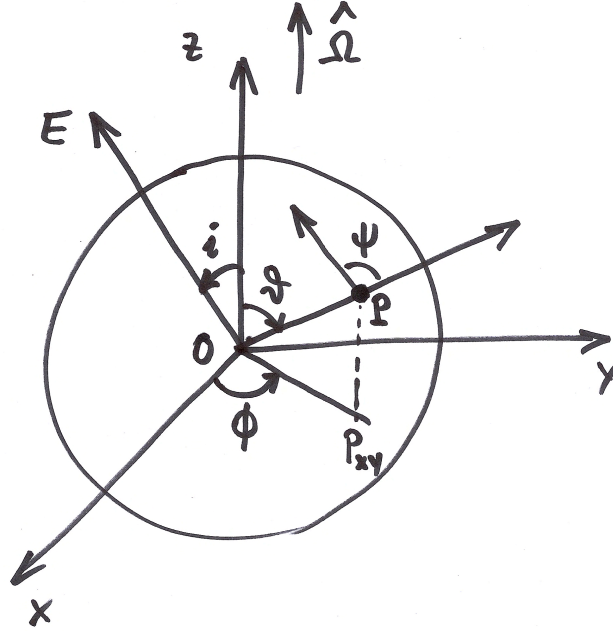
Fig. 1. Illustration of the geometry adopted to compute the spot modeling in the case of a single spherical star. The reference frame has its origin at the barycentre O of the star; the z-axis is along the stellar angular velocity Ω; the xy plane coincides with the equatorial plane of the star with the x-axis chosen so that the line of sight is in the xz plane. The spherical coordinates of a point P on the surface of the star are the colatitude θ and the longitude ϕ. The inclination of the stellar rotation axis to the line of sight is i, while ψ is the angle between the normal in P and the line of sight. The projection of the point P on the equatorial plane of the star is indicated with P_{xy} and is introduced to define the longitude ϕ measured with respect to the x-axis.

If A is the area of a surface element of the photosphere, we define the filling factor of the spots f_s and that of the faculae Qf according to the relationships:

$$A_s \equiv f_s A, \quad A_f \equiv Qf_s A = QA_s, \tag{6}$$

and their intensity contrasts as:

$$c_s \equiv \left(1 - \frac{I_s}{I_u}\right), \quad c_f \equiv -\left(1 - \frac{I_f}{I_u}\right), \tag{7}$$

where the specific intensity of the spot I_s and of the faculae I_f are given at the same point of the photosphere as the unperturbed intensity I_u. The solar faculae are more contrasted towards the limb and virtually invisible at disc centre. For the sake of simplicity, we assume a linear dependence of their contrast on μ (cf.

Lanza et al. 2003, 2004):

$$c_{\mathrm{f}} = c_{\mathrm{f0}}(1 - \mu), \qquad (8)$$

so that

$$\Delta F = A_{\mathrm{s}} I_{\mathrm{u}}(\mu) \left[-c_{\mathrm{s}} + Q c_{\mathrm{f0}}(1 - \mu) \right] \mu = f_{\mathrm{s}} A \, I_{\mathrm{u}}(\mu) \left[-c_{\mathrm{s}} + Q c_{\mathrm{f0}}(1 - \mu) \right] \mu. \qquad (9)$$

In addition, to further simplify our model, we assume that the spot area A_{s} and the contrasts c_{s} and c_{f0} are constant as well as the ratio of the facular-to-spotted area $Q = A_{\mathrm{f}}/A_{\mathrm{s}}$. We also neglect the presence of the spot penumbra as in the first simple models of the variation of the solar irradiance (e.g., Chapman et al. 1984).

The observed flux at the time t is:

$$F(t) = F_{\mathrm{u}} + \Delta F(t), \qquad (10)$$

where the time dependence of ΔF comes from the rotation of the star that changes the projection factor μ. Therefore, the relative variation of the flux according to Eq. (9) is:

$$\frac{F(t)}{F_{\mathrm{u}}} = 1 + \frac{\Delta F(t)}{F_{\mathrm{u}}} = 1 + \frac{A_{\mathrm{s}} I_{\mathrm{u}}(\mu)}{F_{\mathrm{u}}} \left[Q c_{\mathrm{f0}}(1 - \mu) - c_{\mathrm{s}} \right] v(\mu)\mu, \qquad (11)$$

or, substituting Eqs. (2) and (4) into Eq. (11):

$$\frac{F(t)}{F_{\mathrm{u}}} = 1 + \left(\frac{A_{\mathrm{s}}}{\pi R^2} \right) \left(\frac{a + b\mu + c\mu^2}{a + 2b/3 + c/2} \right) \left[Q c_{\mathrm{f0}}(1 - \mu) - c_{\mathrm{s}} \right] v(\mu)\mu, \qquad (12)$$

where the time dependence of the projection factor is given by Eq. (1) and v is the *visibility* of the surface element centered at the point P defined as:

$$v(\mu) = \begin{cases} 1 \text{ if } \mu \geq 0 \\ 0 \text{ if } \mu < 0. \end{cases} \qquad (13)$$

An illustration of the typical rotational modulation produced by our model active region is given in Fig. 2. When the active region is on the invisible hemisphere, the flux is constant at the unperturbed value. When stellar rotation brings the active region into view, the flux initially rises because faculae are more contrasted close to the limb and their dark spots have little effect owing to the foreshortening. As the active region moves towards the centre of the disc, the effect of the faculae becomes less important owing to the decrease of their contrast, while dark spots become dominant as their projected area rises towards disc centre. Finally, when the active region moves toward the other limb, the flux increases again due to the prevailing effect of the faculae.

When a star is much more active than the Sun, its active regions cannot be treated as point-like features. This is the case of young rapidly rotating stars or of the active components of close binaries that were monitored from the ground thanks to their large light curve amplitudes reaching up to 0.2-0.3 mag in the optical passband (Strassmeier et al. 1997; García-Alvarez et al. 2011). In this
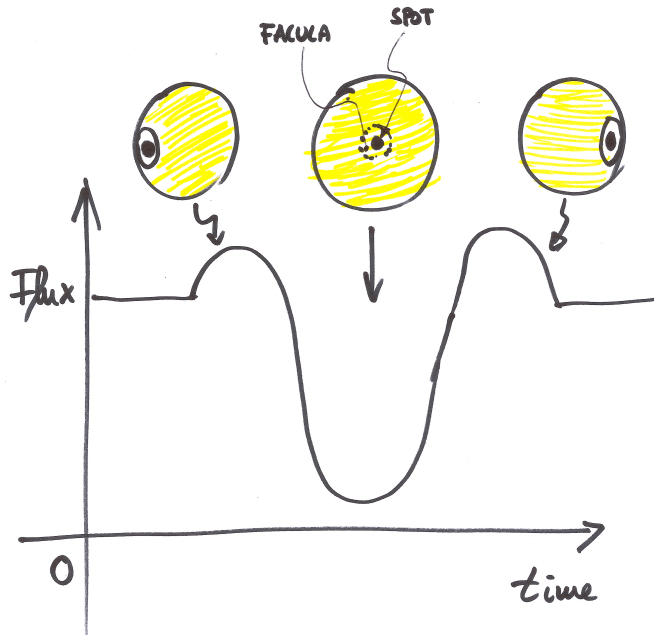
Fig. 2. Illustration of the rotational modulation of the flux produced by a single active region consisting of a dark spot and a bright facular area around it with solar-like contrasts.

case, active regions were generally treated as spherical caps, as discussed in, e.g., Rodonò et al. (1986), Dorren (1987), or Eker (1994). We shall not consider the theory of the light variations produced by such extended spots, referring the interested reader to those works and the references therein. However, a few results obtained with those models will be mentioned in Sect. 2.3.

An important geometrical parameter affecting starspot modelling is the inclination of the stellar spin axis i. If the photometric period $P_{\rm rot}$ is known from timeseries photometry, the rotational broadening of the spectral lines $v \sin i$ is measured from high-resolution spectroscopy, and the radius of the star R is estimated from models or interferometry, we can derive the inclination from: $\sin i = P_{\rm rot}(v \sin i)/2\pi R$. This method can be applied to young rapidly rotating stars because for stars similar to the Sun the relative error on $v \sin i$ is of $\approx 50 - 100$ percent due to the effects of macroturbulence, even when very high-resolution spectra are available. Moreover, for those rapidly rotating stars, the inclination can be derived by minimizing systematic errors in the process of constructing Doppler imaging maps (e.g., Rice & Strassmeier 2000). For stars that rotate slowly, the inclination is generally unknown or can be estimated with large uncertainties. An intermediate case is that of stars that rotate with $\Omega \geq (2-3)\Omega_\odot$ for which asteroseismology can be applied to derive the inclina-

tion because the visibility of the p-modes belonging to a given rotationally split multiplet, that differ by the azimuthal order m, depends on the inclination (e.g., Ballot et al. 2006, 2011).

The role of the faculae is parametrized by Q in our simple model. In general, light variations in stars remarkably more active than the Sun seem to be dominated by dark spots (Lockwood et al. 2007) and also in the Sun the relative contribution of the faculae decreases during the maximum phase of the 11-yr cycle (e.g. Foukal 1998). The recent works by Gondoin (2008) and Messina (2008) provide more information on the facular contribution. A method to estimate Q from single-band light curves, thanks to the different shapes of the facular and spot light modulations, was introduced by Lanza et al. (2003), and its applications are mentioned in Sect. 2.3.

We have considered the case of photometry in a single passband because space-borne telescopes generally observe in a single wide passband to maximize the flux and reduce the photon-shot noise when searching for planetary transits, or have a few non-standardized passbands, such as CoRoT (Auvergne et al. 2009). However, ground-based photometry is often acquired in several standard photometric passbands that allow to estimate the spot temperature (e.g., Poe & Eaton 1985; Strassmeier & Olah 1992). For this application, it is important an appropriate modelling of the limb-darkening in the different passbands. In Fig. 3, the synthetic light curves produced by a starspot on a solar-like star in two different passbands are plotted. The spot is completely dark, that is no flux is coming from it. Therefore, the observed colour variation is due solely to the different limb-darkening coefficients in the two passbands and amounts to ≈ 10 percent of the amplitude of the light modulation. Therefore, a word of caution is in order when interpreting colour modulations as immediate proxies for starspot temperature. If the intrinsic flux of the spot in the considered passbands is low, as it is often the case in the U or B passbands, the colour variation can be dominated by differential limb darkening rather than by the spot temperature deficit.

2.3   Few-spot models

The light curves of a spotted star are generally not sinusoidal, therefore a single spot is not enough to obtain an adequate fit. The simplest models consider two or three non-overlapping spots. In order to compute those models, it suffices to add the effects of individual active regions as introduced in Sect. 2.2. For the case of two spots, the free parameters are: the inclination i, the rotation period $P_{\rm rot} = 2\pi/\Omega$, the limb-darkening coefficients, the unperturbed flux level $F_{\rm u}$, the spot and facular contrasts $c_{\rm s}$ and $c_{\rm f0}$, the ratio of the facular-to-spotted areas Q; and, for each spot, the relative area $A_{\rm s}/\pi R^2$, the colatitude θ, and the initial longitude ϕ_0. The unperturbed level is generally unknown, so it is usually fixed at the maximum observed flux or allowed to vary by $0.1-1$ percent above that level because this can sometimes improve the best fit by providing the model with an additional degree of freedom that allows it to converge to a deeper minimum in the χ^2 landscape. The parameters i, $P_{\rm rot}$, and Q are generally fixed and only
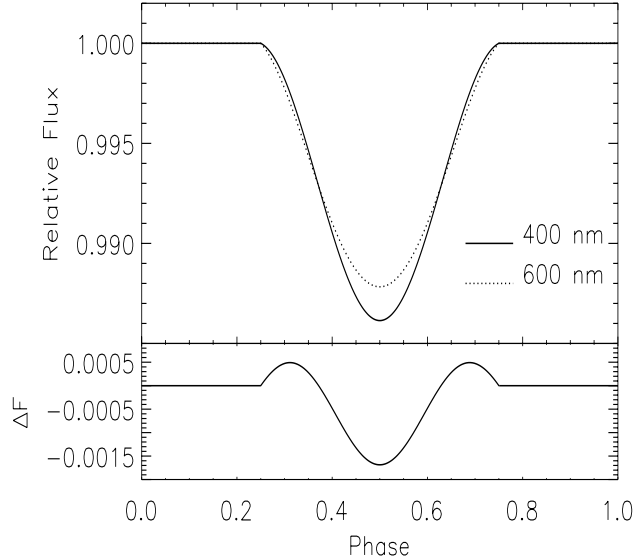
Fig. 3. Upper panel: Synthetic flux vs. rotation phase at two wavelengths (400 and 600 nm) in the case of a completely dark starspot transiting across the disc of a late-type star. The two light curves are different because of the dependence of the limb-darkening coefficients on the wavelength. Lower panel: the flux difference (colour) vs. the rotation phase.

the *geometrical parameters*, i.e., $A_{\rm s}$, θ, and ϕ_0 for each of the spots, are varied to minimize the χ^2 of the model. Sometimes, a flux term independent of the spot longitude is added to the model to account for a uniformly distributed pattern of spots that does not produce any flux modulation, but affects the mean light level (cf. Lanza et al. 2003).

In some cases, thanks to the small number of varied parameters, the model may be unique, for example, a well-defined minimum of the χ^2 can be found in the six-parameter space of a two-spot model. However, in most of the cases, degeneracies among the parameters are present, especially when the accuracy of the photometry is limited. This can be understood if one considers for simplicity a model with only one dark spot without faculae ($Q = 0$). The minimum of light corresponds to the transit of the spot on the central meridian of the star's disc and it allows us to derive the initial longitude of the spot ϕ_0. The minimum of light occurs at time $t_{\rm m}$ when $(t_{\rm m} - t_0) = -\phi_0/\Omega$ and its amplitude is: $|\Delta F|_{\rm max}/F_{\rm u} = c_{\rm s}(A_{\rm s}/\pi R^2)\cos(i - \theta)$, where limb-darkening is neglected for simplicity. The duration of the spot transit δt corresponds to the two longitudes where $\mu = 0$, i.e., $\delta t = t_2 - t_1$, where $\sin i \sin \theta \cos[\phi_0 + \Omega(t_i - t_0)] + \cos i \cos \theta = 0$,

with $i = 1, 2$. Therefore, if the inclination $i \neq 90°$, the unspotted flux level F_{u}, and the other physical parameters are known, we can derive the three geometrical parameters A_{s}, θ, and ϕ_0 of our single spot from the duration δt, the time of light minimum t_{m}, and the amplitude of the light minimum $|\Delta F|_{\mathrm{max}}/F_{\mathrm{u}}$. If the inclination is $90°$, the duration δt of the transit of the spot across the disc becomes independent of its colatitude and we loose the information on that parameter. Even if $i \neq 90°$, the finite precision of the photometry induces uncertainties on the spot location and area. If the inclination i is not known a priori, the colatitude θ, the unprojected area A_{s}, and the inclination i itself become largely degenerate because the combination $A_{\mathrm{s}} \cos(i - \theta)$ appears in the relationship for the amplitude of the flux modulation. These considerations show that spot modelling can give unique solutions only in very special cases.

When we fit two spots and the inclination is only poorly estimated, we expect strong degeneracies to arise among the different parameters because different combinations of the individual spot areas and colatitudes give similar light modulations, especially when the inclination is close to $90°$. In spite of such limitations, two-spot models have been widely applied to fit ground-based photometry for which the precision is of the order of 0.01 mag. To obtain a sufficient coverage in phase, the data gathered along an entire season were generally used to construct an average light curve, thus averaging short-term changes in the spot pattern. Rodonò et al. (1986) provided some examples of that kind of spot models, generally yielding a well-defined minimum in the χ^2 space thanks to the limited number of free parameters. Spots at high latitudes and even at the poles were often found because the model used them to adjust the variations of the mean light level given that they were circumpolar for inclination $i \neq 90°$ and therefore always in view.

Recently, two-spot models have been resumed and applied within a Bayesian framework using Monte Carlo Markov Chain techniques to fully explore the a posteriori parameter distributions and their degeneracies (Croll 2006; Fröhlich 2007; Lanza et al. 2014). The applications were focussed on estimating the amplitude of the surface differential rotation by allowing the two spots to have different rotation periods. A two-spot model with non-evolving spots was applied to individual time intervals sufficiently short to avoid that the intrinsic spot evolution affects the result.

Other applications of models with a few spots are the estimation of the facular-to-spotted area ratio Q or of the maximum time interval during which the spot pattern is unaffected by the intrinsic starspot evolution. Lanza et al. (2003) first performed those applications for the Sun and then for some CoRoT and Kepler targets (cf. Lanza et al. 2009a,b, 2010, 2011; Bonomo & Lanza 2012). Note that, since Q appears in combination with the facular contrast parameter c_{f0} in the product $Q c_{\mathrm{f0}}$ (cf. Eq. 12), it is possible to determine Q only by fixing c_{f0}.

2.4   Multispot models with evolution

The advent of automated photometric telescopes in the '90s allowed to follow the evolution of the light modulation of active stars in a systematic way and posed the problem of modelling their spot evolution (e.g. Rodonò et al. 2001). Strassmeier & Bopp (1992) were among the first to propose a model that incorporated the intrinsic evolution of the starspots and the relative drift in latitude owing to surface differential rotation. With space-borne telescopes such as CoRoT, multi-spot models with evolution became even more important. Mosser et al. (2009) fitted the light curves of several CoRoT asteroseismic targets by applying a model with evolving spots, usually limited to $2-3$ per stellar rotation. Best fits were obtained with an extended exploration of the geometric parameter space by means of a relaxed χ^2 minimization based on a technique similar to simulated annealing. Their method was extensively tested with simulated data and compared to other approaches to study the dependence of the results on model assumptions and on the parameters held fixed. The model proved useful to derive robust estimates of the spot lifetimes and mean rotation period, while other parameters, such as the inclination of the spin axis (independently known from asteroseismology), spot latitudes, and differential rotation were found sensitive to model assumptions.

Frasca et al. (2011) and Fröhlich et al. (2012) (cf. also Fröhlich et al. 2009), applied multispot models with up to $7-9$ evolving spots to fit Kepler timeseries of several hundred days. A Bayesian approach was used to derive the a posteriori free parameter distributions generally including the inclination and the surface differential rotation.

The main limitation of multi-spot models, in addition to the strong parameter degeneracies, is the large amplitude of the residuals in comparison with the photometric errors. This is especially critical when we model the light curves of eclipsing binaries because the eclipse profile is highly sensitive to the shape and location of the occulted spots. For these reasons, continuous spot models, similar to those considered for Doppler imaging (Vogt et al. 1987), have been introduced since the second half of the '90s to improve the best fits of the light curves. They will be the subject of the next sections.

3   Models with continuous spot distributions

A continuous distribution of spots on the surface of a star can be specified by giving the spot filling factor f_s in each surface element. We define $f_\mathrm{s} \equiv A_\mathrm{s}/A$, where A_s is the spotted area within the surface element of area A, as considered above. The spot distribution is mapped by the distribution of f_s over the surface of the star. Since the light curve is a one-dimensional dataset, while the filling factor map is a two-dimensional function, i.e., $f_\mathrm{s} = f_\mathrm{s}(\theta, \phi)$, the problem of finding f_s given the light curve has generally many different solutions and the map is also highly sensitive to small variations in the input dataset. In the mathematical language, this is a *ill-posed problem* (cf. Tikhonov & Goncharsky 1987).

The usual method to solve this kind of problems is by combining the information coming from the light curve with some a priori information in order to obtain a unique and stable solution, i.e., a map that does not vary greatly when there are small variations in the dataset, or, in other words, that is not critically sensitive to the effect of the errors in the photometry. A simple way of introducing a priori assumptions in the solution process is by restricting the shape and number of the spots, as we did in the previous discrete spot models. A more sophisticated way is that of coding some statistical property that we want to impose to the solution into an appropriate functional. This is the method of *solution regularization* that will be described below. However, before introducing the mathematical formulation of regularization, we need to compute the flux emergent from the stellar disc in the presence of a continuous spot distribution.

3.1 Flux variation produced by a continuous distribution of active regions

For simplicity, we subdivide the surface of the star into a large number of elements N, each of area A_k, where $k = 1, ..., N$. The flux coming from the k-th element is:

$$\delta F_k = I(\mu_k) A_k \mu_k v(\mu_k), \tag{14}$$

where

$$I(\mu_k) = f_s I_s + Q f_s I_f + [1 - (Q+1) f_s] I_u(\mu_k). \tag{15}$$

This equation gives the average specific intensity emerging from the given surface element as the result of the intensity coming from the spotted photosphere with a filling factor f_s, from the facular photosphere with a filling factor $Q f_s$, and from the unperturbed photosphere, the filling factor of which is $1 - (Q+1) f_s$. With little algebra, we find:

$$I(\mu_k) = \{1 + [c_{f0} Q(1 - \mu_k) - c_s] f_s\} I_u(\mu_k). \tag{16}$$

The total flux coming from the disc is:

$$F(t) = \sum_{k=1}^{N} \delta F_k = \sum_k A_k I_u(\mu_k) \{1 + [c_{f0} Q(1 - \mu_k) - c_s] f_k\} v(\mu_k) \mu_k, \tag{17}$$

where f_k is the spot filling factor (previously indicated with f_s), μ_k the projection factor of the k-th surface element at the time t (cf. Eq. 1), and $v(\mu_k)$ the visibility function in Eq. (13).

In general, we want to compute M flux values $F_j \equiv F(t_j)$, where t_j are the times of the observations, with $j = 1, ..., M$; we define them as the model flux vector $\mathbf{F} \equiv \{F(t_j), j = 1, ..., M\}$. We can express its relationship to the distribution of the filling factor on the surface of the star by introducing an $M \times N$ projection matrix $\tilde{\mathbf{R}} = \{R_{jk}\}$ and a constant vector C_u such as:

$$F_j \equiv F(t_j) = \sum_k R_{jk} f_k + C_{uj}, \tag{18}$$

or, in matrix notation:
$$\mathbf{F} = \tilde{\mathbf{R}}\mathbf{f} + \mathbf{C}_{\mathrm{u}}, \tag{19}$$

where $\mathbf{f} = \{f_k, \ k = 1, ..., N\}$ is the vector of the filling factor on the surface of the star and

$$R_{jk} \equiv A_k I_{\mathrm{u}}(\mu_k) \left[c_{f0}Q(1 - \mu_k) - c_{\mathrm{s}}\right] v(\mu_k)\mu_k \ \text{ with } \mu_k = \mu_k(t_j), \tag{20}$$

and

$$C_{\mathrm{uj}} \equiv A_k I_{\mathrm{u}}(\mu_k)v(\mu_k)\mu_k + F_{\mathrm{uj}}, \tag{21}$$

(cf. 17) where we introduce the vector of the unperturbed flux $\mathbf{F}_{\mathrm{u}}$ consisting of M constant components, i.e., $\mathbf{F}_{\mathrm{u}} \equiv \{F_{\mathrm{uj}}, j = 1, ..., M\}$ with $F_{\mathrm{uj}} = F_{\mathrm{u}}$.

3.2   The light curve inversion problem and the regularization

We now consider the inverse problem of deriving the distribution of the spot filling factor from the light curve dataset. If the observed flux values at the times t_j are denoted as the vector $\mathbf{D} = \{D_j, \ j = 1, ..., M\}$, we can first consider the ideal case when: a) there are no measurement errors; b) our model for the flux variations is exact; and c) the unspotted flux is known. In this case, one may hope to derive a solution for the filling factor vector $\mathbf{f}$, by solving the linear system:
$$\tilde{\mathbf{R}}\mathbf{f} = \mathbf{D} - \mathbf{C}_{\mathrm{u}}. \tag{22}$$

In general, this system has infinite solutions because the matrix $\tilde{\mathbf{R}}$ is singular, i.e., it has a nullspace of finite dimension whose vectors $\mathbf{f}_{\mathrm{null}}$ have the property $\tilde{\mathbf{R}}\mathbf{f}_{\mathrm{null}} = 0$ (see Press et al. 2002, Ch. 2). Therefore, if a given vector $\mathbf{f}_0$ is a solution of Eq. (22), $\mathbf{f}_0 + h\mathbf{f}_{\mathrm{null}}$, where h is any real number, is a solution too. Cowan et al. (2013) investigated the nullspace in some light curve inversion problems showing that it can significantly affect the solution. From a geometrical point of view, the existence of the null space is associated with particular distributions of brightness on the stellar surface that do not produce a light modulation as the star rotates (see Cowan et al. 2013, for some examples).

   A more realistic case is that of a dataset with finite errors. In this case, we look for a solution that minimizes the χ^2 between the dataset and the model. Specifically, the χ^2 corresponding to a given distribution of the filling factor is:

$$\chi^2(\mathbf{f}) \equiv \sum_{j=1}^{M} \frac{(D_j - F_j)^2}{\sigma_j^2}, \tag{23}$$

where σ_j is the standard deviation of the flux measurement D_j.

   In general, the solution found by minimizing the χ^2 is not unique and is highly sensitive to small changes in the dataset, in the sense that a small change in the data vector $\mathbf{D}$ produces a large change in the filling factor distribution $\mathbf{f}$. The idea of regularization is to add to the χ^2 an appropriate mathematical function of $\mathbf{f}$ that warrants a unique and stable solution, i.e., a solution that

varies in a continuous way in the $\mathbf{f}$ space. Note that in general the filling factor is a function $f(\theta, \phi)$ that we have discretized into a vector $\mathbf{f}$ of N elements, therefore the regularizing term is, mathematically speaking, a functional. There are several possible choices that have been investigated by the mathematicians and proved effective in our kind of inversion problem (cf. Tikhonov & Goncharsky 1987; Titterington 1985).

The most widely used is the maximum entropy functional that provides a quantitative measure of the configuration entropy of the map, i.e., of the information necessary to transmit the map expressed as a sequence of bytes (Bryan & Skilling 1980; Narayan & Nityananda 1986). It assumes a default map as a reference and measures the difference in the information content of the considered map with respect to it. In our case, the default map corresponds to an immaculate star. The specific formulation of the maximum entropy functional that I prefer is that given by Collier Cameron (1992).

The regularized solution is computed by minimizing an objective function Z defined as a linear combination of the χ^2 and the regularizing functional S. For the maximum entropy case:

$$Z(\mathbf{f}) = \chi^2(\mathbf{f}) - \lambda_{\mathrm{ME}} S(\mathbf{f}), \tag{24}$$

where $\mathbf{f} = \{f_k, \ k = 1, ...N\}$ is the vector of the spot filling factors for the individual surface elements, $\lambda_{\mathrm{ME}} > 0$ a Lagrangian multiplier, and

$$S = -\sum_k w_k \left[f_k \log \frac{f_k}{m} + (1 - f_k) \log \frac{(1 - f_k)}{(1 - m)} \right], \tag{25}$$

is the entropy functional, where w_k is the relative area of the k-th surface element and $m = 10^{-6}$ is a default minimum spot filling factor included to avoid the divergence of the logarithm. S gets its maximum value equal to zero for an immaculate star, i.e., $f_k = m$ in each surface elements.

The effect of the regularization is that of reducing the spot filling factor (or the spotted area) as much as possible, compatibly with fitting the data, by increasing the Lagrangian multiplier. In Fig. 3.2, we show the isocontours of the χ^2 landscape for the illustrative case of a map consisting of only two surface elements that we use to explain the concept. Without regularization (i.e., $\lambda_{\mathrm{ME}} = 0$), the best fit has the minimum $\chi^2 = \chi_0^2$ and the residuals of the fit have a Gaussian distribution with a mean value $\mu = 0$ and a standard deviation σ_0. In general, the best fit with $\chi^2 = \chi_0^2$ is not acceptable because we fit also some component of the measurement errors and the solution is unstable. With the regularization, ($\lambda_{\mathrm{ME}} > 0$), the fit has $\chi^2 = \chi_1^2 > \chi_0^2$ and the residual distribution is now centred at a value $\mu < 0$ because the spotted area is reduced. However, the solution becomes stable and unique for a sufficiently large value of λ_{ME}.

The role of the a priori information introduced through the regularization is that of selecting one specific solution vector $\mathbf{f}$ among the infinite ones that correspond to the condition $\chi^2 = \chi_1^2$. In the case of the maximum entropy solution, the selected vector $\mathbf{f}$ corresponds to the solution that minimizes the individual

f_k, while verifying the condition $\chi^2 = \chi_1^2$. Of course, it is possible to move along a different line in the χ^2 landscape which corresponds to a different kind of regularization. The fundamental requisite for the choice of the regularizing functional is that it must lead to a unique and stable solution when the Lagrangian multiplier λ is sufficiently large.
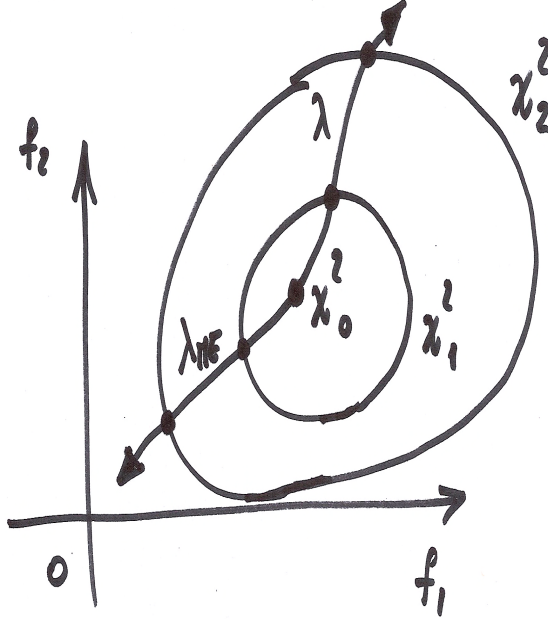

Fig. 4. The χ^2 landscape in the case of a simple model with only two surface elements $\mathbf{f} = \{f_1, f_2\}$, showing the minimum of the χ^2, i.e., χ_0^2, and the effect of the regularization ($\lambda_{\mathrm{ME}} > 0$) that increases the χ^2 value, driving at the same time the solution towards the unspotted map with $\mathbf{f} = 0$. The effect of a different regularizing functional that moves the solution along a different path is also shown for comparison.

In the case of the maximum entropy regularization, we fix the optimal value of λ_{ME} by comparing μ with σ_0, the standard deviation of the residuals as obtained with the unregularized best fit (i.e., for $\lambda_{\mathrm{ME}} = 0$). The signal-to-noise ratio of a light curve can be defined as $S/N = \mathcal{A}_{\max}/\sigma_0$, where $\mathcal{A}_{\max}$ is the maximum amplitude of the light modulation due to the starspots. By increasing λ_{ME}, the fit is shifted towards the unspotted level (see Fig. 3.2), while the distribution of the residuals is shifted towards negative values and its standard deviation σ increases because the regularization smooths out the small spots that were previously used to fit the noise components and reduce the χ^2 (see Fig. 3.2). A practical recipe to fix λ_{ME} in the case of photometry with high signal-to-noise
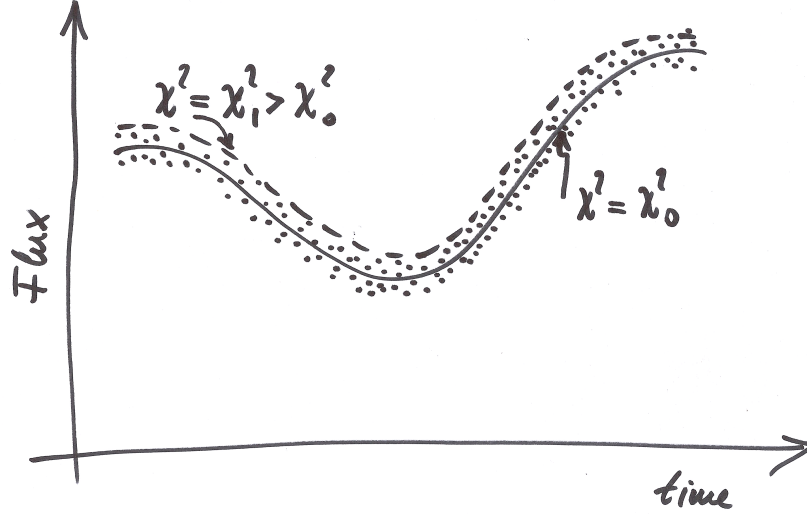
Fig. 5. Illustration of the best fit of a light curve without regularization (solid line) with $\chi^2 = \chi_0^2$ and with regularization having $\chi^2 = \chi_1^2 > \chi_0^2$ (dashed line). The latter is higher than the best fit corresponding to the minimum of the $\chi^2 = \chi_0^2$ and its residuals are not symmetrically centred on the zero value because the regularization smooths out the spot pattern driving the solution towards the unspotted flux level, here assumed to be higher than the light maximum.

$(S/N \geq 100)$ consists in increasing λ_{ME} until:

$$\mu = \frac{\sigma_0}{\sqrt{M}}, \qquad (26)$$

where M is the number of data points in the light curve (cf. Lanza et al. 2009a). When $S/N \approx 10 - 30$, we need to adopt a stronger regularization to reduce the impact of the noise, i.e.:

$$\mu = \beta \frac{\sigma_0}{\sqrt{M}}, \qquad (27)$$

where $1.5 \leq \beta \leq 3$ is a numerical factor (cf. Lanza et al. 2009b). A visual inspection of the fit is generally needed to find the largest possible acceptable deviations, i.e., to fix the appropriate value of β by considering the trade-off between the accuracy of the fit and its smoothness.

Another regularizing functional often adopted is the Tikhonov functional T. It selects the smoothest map compatible with the data, i.e., the one that minimizes the average $|\nabla f(\theta, \phi)|^2$ over the stellar surface (Piskunov et al. 1990).
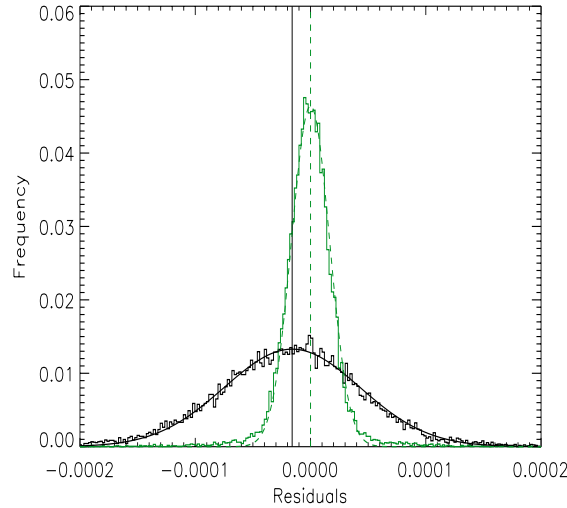
Fig. 6. Distribution of the residuals of the best fit of a light curve obtained without any regularization (green histogram) together with its Gaussian best fit (green dashed line) centred at zero value, as indicated by the dashed green vertical line. The distribution of the residuals after applying the maximum entropy regularization is shown by the black histogram together with its Gaussian best fit (black solid line); the solid vertical line marks the mean of the Gaussian best fit. Note that the distribution of the residuals of the regularized solution is centred at a negative value because the corresponding fit is systematically higher than the photometric data points as shown in Fig. 3.2. Its standard deviation is larger than that of the unregularized solution because the spot pattern is smoother owing to the regularization.

In other words, one seeks to minimize a linear combination $Z = \chi^2 + \lambda_{\mathrm{T}} T$, where $\lambda_{\mathrm{T}} > 0$ is the Lagrangian multiplier and:

$$T(\mathbf{f}) = \int_{\Sigma} \left[\left(\frac{\partial f}{\partial \theta} \right)^2 + \frac{1}{\sin^2 \theta} \left(\frac{\partial f}{\partial \phi} \right)^2 \right] d\Sigma, \qquad (28)$$

where Σ is the surface of the star whose element is $d\Sigma = \sin \theta d\theta d\phi$. Of course, other regularizing functionals are possible, e.g., that introduced by Harmon & Crews (2000) and applied by Roettenbacher et al. (2013).

A crucial limitation of spot modelling is that we use 1-D information, that is, a light curve, to reconstruct a 2-D map of the stellar surface. Most of the applications of regularized spot modelling have targeted close eclipsing binaries or, more recently, active stars with transiting planets whose inclination is close to

$90°$. Therefore, the information on spot latitude is very limited or non-existent. In those cases, it is better to collapse the 2-D map obtained by a regularized model into a 1-D distribution of the spot filling factor versus the longitude and consider that distribution as the final product of the modelling. The *relative variation* of the spotted area vs. the longitude has little dependence on the specific regularization adopted and can be considered as a robust result of the analysis (cf. Lanza et al. 1998, 2006). In other words, the absolute value of the spotted area depends on the often unknown spot contrast and unspotted light level, but its relative distribution vs. longitude can be derived thanks to the light modulation that it produces as the star rotates. Similarly, the long-term variations in the relative spotted area can be considered a robust result of the modelling, if we assume that the spot contrast stays constant in the given passband. This allows us to detect stellar activity cycles akin to the 11-yr sunspot cycle.

3.3   Alternative approaches

The minimization of the χ^2 can be approached also by means of the *singular value decomposition* (hereafter SVD) of the projection matrix $\tilde{\mathbf{R}}$. The method is described in, e.g., Press et al. (2002). The main advantage is that the linear combinations of the components of $\mathbf{f}$ that are not constrained by the data are driven to zero or to small, insignificant values, while the solution becomes dominated by the linear combinations of the elements of $\mathbf{f}$ that can account for most of the flux variation. These are the so-called *principal components*. The number of components retained in the solution is determined by the minimum acceptable singular value. An advantage of the method is that the errors of the individual components can be evaluated starting from the errors of the individual photometric data. In the case of the regularized models, the statistical errors on the f_k are not easily estimated because the a priori information introduced into the solution usually dominates. Therefore, systematic errors can be larger than the statistical errors in most of the cases and only a comparison between maps obtained with different regularizing functionals provides some insight into the errors (Lanza et al. 1998).

Several spot modelling approaches based on the general principle of SVD or principal component analysis have been proposed, e.g., by Berdyugina (1998) or Savanov & Strassmeier (2005, 2008) who also performed comparisons with test cases and studied the general properties of the solutions.

Finally, it is worth mentioning the approach by Cowan et al. (2013) who applied a Fourier decomposition method to extract a map from the observed rotational flux modulation. In principle, all the Fourier components of the spot map characterized by different azimuthal orders m can be extracted in the case of an ideal noiseless light curve sampled with perfect continuity. In practice, their amplitude decreases as $|m^2 - 1|^{-1}$ for $m > 1$. This implies that in the case of a real light curve, the amplitudes of the higher order Fourier components become soon comparable with or smaller than the noise, making it impossible to accurately extract them. In other words, it becomes impossible to resolve

sufficiently localized brightness inhomogeneities. For this reason, a model based on a discrete (or continuous) spot distribution is generally superior to Fourier decomposition in the case of active stars.

4   Spot occultations during planetary transits

The observations of extrasolar planets transiting their host stars opened a new avenue in the investigation of other planetary systems. Here, I shall consider only the contribution that planetary transits give to the modelling of the distribution of the surface brightness on the disc of their host stars. In Fig. 4, the case of a planet transiting across the disc of a star with a dark spot along the occulted band is shown, neglecting for simplicity the effects of the limb darkening. When the planet's disc is not covering the spot, the flux is reduced by the spot, but the variation of the flux vs. the time has exactly the same shape as when the spot is not on the stellar disc. However, when the spot is occulted by the planet, the flux shows a relative increase because the configuration corresponds to that of a planet transiting across the disc of a star without spots, that is, whose flux is higher. The position of the centre of the light bump gives a measure of the spot longitude on the stellar disc, while its extension gives a measure of the size of the spot, or, to be precise, of the extension in longitude of the portion of the spot that is occulted by the planet (e.g., Wolter et al. 2009). Finally, the amplitude of the bump depends on the contrast of the spot that can provide a measure of its temperature when the effective temperature of the unperturbed photosphere is known. Silva-Valio et al. (2010) determined the distributions of the size and contrast of the spots occulted in CoRoT-2 using this approach. This method is unique to resolve small spots (~ 50 Mm) on slowly rotating, sun-like stars that cannot be mapped through Doppler imaging techniques. In principle, spots as small as a few Mm can be resolved if an Earth-size planet occults them, although the photometric accuracy of CoRoT and Kepler is generally insufficient to do that on individual transits (cf. Barros et al. 2014).

Starspot occultations can be used to derive the rotation rate of the star in the latitude band occulted by the planet, if the orbit of the planet and the equator of the star are aligned, because successive occultations of the same spot along successive transits can be used to precisely measure the variation of its longitude vs. the time (Silva-Valio 2008). On the other hand, is the stellar spin and the orbital angular momentum are not aligned, the planet cannot occult the same spot along successive transits because the rotational motion of the spot across the stellar disc is not parallel to the transit chord (Nutzman et al. 2011; Sanchis-Ojeda & Winn 2011; Sanchis-Ojeda et al. 2013). Therefore, monitoring starspot occultations along successive transits can provide information on the projected alignment of the stellar spin and orbital angular momentum in a planetary system. Similar information can be obtained through the observation of the radial-velocity anomaly induced by the transit, i.e., the so-called Rossiter-McLaughlin effect, that allows a measurement of the projected misalignment, although limited to stars with a $v \sin i \geq 2 - 3$ km s^{-1} (e.g., Albrecht et al.
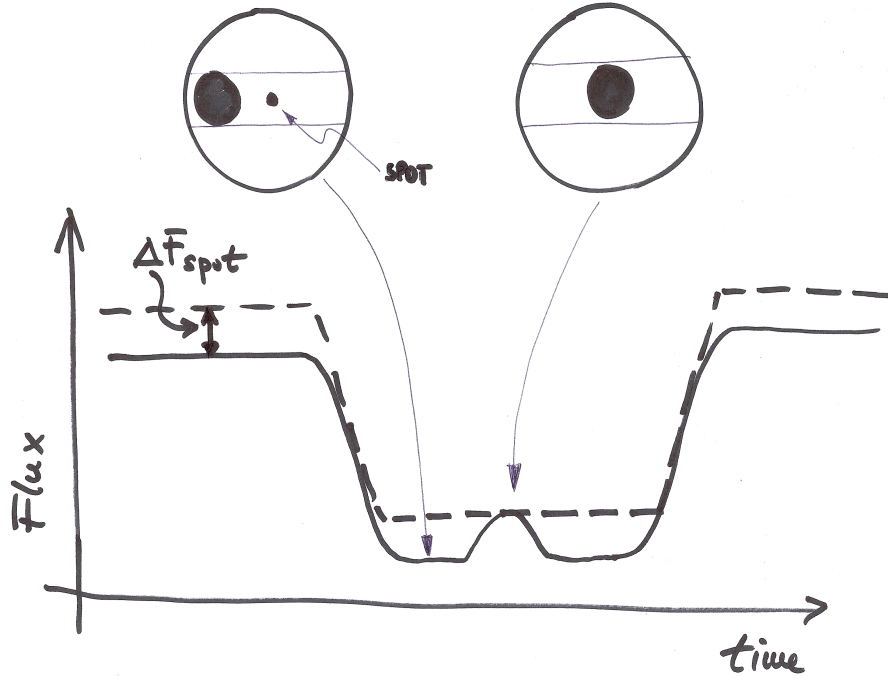
Fig. 7. The case of a transiting planets occulting a dark spot (at the disc centre) along the transit chord. The flux variation due to the transit in the case of a star with the spot is given by the solid line in the lower plot that shows a relative flux increase (a bump) when the spot is occulted. This happens because the corresponding configuration is the same as in the case without spot. In that case the reference flux level outside the transit is higher as shown by the dashed line that is the flux variation vs. the time in the case of a star without spots. The quantity ΔF_{spot} measures the flux decrease due to the spot when it is in view on the stellar disc.

2012). Note that different models of planetary system formation predict different misalignment distributions, therefore such a kind of measurements provides stringent tests to those models.

The precise timing of planetary transits should also take into account the distortions of the transit profile due to spot occultations. This can be a subtle effect when the photometric accuracy is not high enough to resolve the individual bumps (Oshagh et al. 2013; Barros et al. 2014).

5   Tests of spot models

Many tests of spot models have been published in the literature since the beginning of their application. Among the classic works, I refer to Kovari & Bartus (1997) for two-spot models. Here, I shall consider only a few tests that are based on a comparison with direct observations in the case of the Sun or with the results obtained with independent methods such as Doppler imaging or starspot occultations during planetary transits.

The total solar irradiance (hereafter TSI) provides a good proxy for the modulation of the Sun as a star because its variation is dominated by photospheric sunspots and faculae that produce most of their effects in the optical passband, although the relative variations becomes larger and larger at shorter and shorter wavelengths, in particular if we consider those associated with the solar cycle. Our star is seen almost equator-on, therefore the TSI light curve does not contain information on the latitudes of the active regions, but only on their longitudes and area variations. Lanza et al. (2007) performed detailed tests for different spot modelling approaches by fitting the TSI modulation over an extended portion of solar cycle 23. They applied three-spot, maximum entropy, and Tikhonov regularized models, and compared the derived distributions of the filling factor vs. longitude with those of observed sunspot groups as well as with the variation of their total area. Adopting a fixed value Q for the facular-to-spotted area ratio, they found a remarkably good reproduction of the longitude distribution of the sunspot groups during the rising and the maximum phase of the cycle with the maximum entropy model performing significantly better than the three-spot and Tikhonov models. The resolution in longitude of the models was about $40° - 50°$ considering a typical $S/N \sim 50 - 100$.

The facular component in the active regions can induce systematic shifts in their derived longitudinal distribution because faculae have a photometric effect that reaches the maximum close to the limb, while dark spots produce their maximum effect closer to the disc centre. Therefore, the model can shift the longitude of a given active region in an attempt to better reproduce the light modulation with the constraint of a fixed Q. The variation in the total spotted area is also systematically affected by the value of Q, but the overall variations due to the solar 11-yr cycle are reproduced, in particular by the maximum entropy models.

Lanza et al. (2007) conclude that the maximum entropy model provides the most precise description of the distribution of the active regions vs. longitude in the Sun, in particular when the $Q = 9$ value they adopted is the most appropriate, that is in the rising and maximum phases of the 11-yr cycle. The good reproduction of the overall variations in the total sunspot area supports the use of that spot modelling to detect stellar activity cycles. The reason why the maximum entropy model is better in comparison to the discrete and Tikhonov models is probably associated with the low level of activity of our star that is characterized by several small active regions simultaneously present on the stellar disc. The three spot models has too few degrees of freedom to account for the complexity of the pattern, especially during the rising and the maximum cycle

phases, while the Tikhonov maps display too smooth and extended features that are not observed on the Sun.

In the case of distant stars, the results of Lanza et al. (2007) support the use of spot modelling to derive active spot longitudes and activity cycles. An independent test by comparing maximum entropy models with an extended sequence of Doppler imaging maps was performed by Lanza et al. (2006) in the case of the highly active close binary HR 1099 for which long-term photometry from the ground was available. The results support the possibility of deriving the distribution of the starspots vs. the longitude, although with a limited resolution ($\approx 100°$) because of an $S/N \sim 10 - 30$ attainable from the ground.

Another interesting test was performed by Silva-Valio & Lanza (2011) in the case of the planetary host CoRoT-2. From the out-of-transit light curve, Lanza et al. (2009a) computed a maximum entropy spot model that provided them with the distribution of the spot filling factor vs. the longitude and time. It was compared with the longitudes of the spots occulted during the transits finding a remarkably good agreement. Although planetary occultations provided a significantly higher longitude resolution, the locations of the active longitudes where starspots were preferentially found were reproduced very well and also their migration vs. the time was very similar.

CoRoT-2 became also a benchmark to test different spot modelling approaches. For example, Huber et al. (2010) considered a model in which the surface of the star was subdivided into 12 non-occulted sectors and 24 sectors along the occulted chord, varying their brightness to fit the light curve. They obtained a spot map remarkably similar to that of Lanza et al. (2009a) that was based on the out-of-transit light curve only, thus confirming their results. Another test came from the comparison with a Bayesian few-spot model by Fröhlich et al. (2009).

Independent confirmations are particular important in view of the results on the active longitudes, spot lifetimes, surface differential rotation, and short-term activity cycles obtained for CoRoT-2 as well as for other stars with close-in transiting planets such as Kepler-17 (Bonomo & Lanza 2012). For a detailed discussions of these topics, I refer to the cited original papers and to Lanza (2014) for the possibility of star-planet interactions affecting stellar photospheric activity.

6   Conclusions

I briefly reviewed the foundations of spot modelling, the relevance of which is becoming increasingly greater thanks to the availability of high-precision, high-duty cycle light curves acquired by space-borne telescopes designed to look for transiting planets around solar-like stars (cf. Rauer et al. 2014). Different mapping techniques can be applied to derive the distribution of the spotted area vs. longitude and its relative time variation with good confidence, especially in the case of stars with transiting planets for which the inclination can be safely derived or reasonably guessed from the measurement of their projected spin-orbit

angle. CoRoT-2 is a benchmark case for the comparison of different modelling approaches as well as for the phenomena that can be detected with spot modelling such as active longitudes, spot evolution, differential rotation, and short-term activity cycles (Lanza et al. 2009a).

I limited myself to the standard spot models proposed for active stars. However, specialized models for stars with transiting and non-transiting planets are expected to become even more important in the near future because they provide information on the spin-orbit alignment of the systems. The radial velocity jitter associated with stellar active regions is a major limitation to the detection and measurement of the mass of Earth-sized planets (e.g. Haywood et al. 2014). Spot modelling techniques can be applied to mitigate its impact as shown by recent investigations (cf. Dumusque 2014; Dumusque et al. 2014, and references therein).

The possibility of extending spot modelling to pre-main sequence stars is also interesting, although limited to those objects the light variations of which are dominated by photospheric brightness inhomogeneities (Cody et al. 2014). Finally, a word of caution is in order in the case of close binary systems where the light modulations due to different effects, such as ellipsoidicity, reflection, gravity darkening, and Doppler beaming can combine with those due to surface brightness inhomogeneities to produce a complex phenomenology the modelling of which is a very challenging task (cf. Lanza et al. 1998; Kallrath & Milone 1999; Herrero et al. 2013, 2014).

Acknowledgment

Bibliography

Albrecht, S., Winn, J. N., Johnson, J. A., et al. 2012, ApJ, 757, 18

Auvergne, M., Bodin, P., Boisnard, L., et al. 2009, A&A, 506, 411

Ballot, J., Gizon, L., Samadi, R., et al. 2011, A&A, 530, A97

Ballot, J., García, R. A., & Lambert, P. 2006, MNRAS, 369, 1281

Barros, S. C. C., Almenara, J. M., Deleuil, M., et al. 2014, A&A, 569, A74

Berdyugina, S. V. 1998, A&A, 338, 97

Berdyugina, S. V. 2005, Living Reviews in Solar Physics, 2, 8

Bonomo, A. S., & Lanza, A. F. 2012, A&A, 547, A37

Borucki, W. J., Koch, D., Basri, G., et al. 2010, Science, 327, 977

Bryan, R. K., & Skilling, J. 1980, MNRAS, 191, 69

Chapman, G. A., Herzog, A. D., Lawrence, J. K., & Shelton, J. C. 1984, ApJ, 282, L99

Chapman, G. A., Dobias, J. J., & Arias, T. 2011, ApJ, 728, 150

Chapman, G. A., Cookson, A. M., Dobias, J. J., & Walton, S. R. 2001, ApJ, 555, 462

Chapman, G. A., Cookson, A. M., & Dobias, J. J. 1994, ApJ, 432, 403

Cody, A. M., Stauffer, J., Baglin, A., et al. 2014, AJ, 147, 82

Collier Cameron, A. 1997, MNRAS, 287, 556

Collier Cameron, A. 1992, Surface Inhomogeneities on Late-Type Stars, 397, 33

Cowan, N. B., Fuentes, P. A., & Haggard, H. M. 2013, MNRAS, 434, 2465

Croll, B. 2006, PASP, 118, 1351

Donahue, R. A., Dobson, A. K., & Baliunas, S. L. 1997, Solar Physics, 171, 211

Donahue, R. A., Dobson, A. K., & Baliunas, S. L. 1997, Solar Physics, 171, 191

Dorren, J. D. 1987, ApJ, 320, 756

Dumusque, X. 2014, ApJ, 796, 133

Dumusque, X., Boisse, I., & Santos, N. C. 2014, ApJ, 796, 132

Eker, Z. 1994, ApJ, 420, 373

Foukal, P., Bernasconi, P., Eaton, H., & Rust, D. 2004, ApJ, 611, L57

Foukal, P. 1998, ApJ, 500, 958

Frasca, A., Fröhlich, H.-E., Bonanno, A., et al. 2011, A&A, 532, A81

Fröhlich, H.-E. 2007, Astronomische Nachrichten, 328, 1037

Fröhlich, H.-E., Küker, M., Hatzes, A. P., & Strassmeier, K. G. 2009, A&A, 506, 263

Fröhlich, H.-E., Frasca, A., Catanzaro, G., et al. 2012, A&A, 543, A146

García-Alvarez, D., Lanza, A. F., Messina, S., et al. 2011, A&A, 533, A30

Gondoin, P. 2008, A&A, 478, 883

Gray, D. F. 2008, The Observation and Analysis of Stellar Photospheres, by David F. Gray, Cambridge, UK: Cambridge University Press, 2008

Harmon, R. O., & Crews, L. J. 2000, AJ, 120, 3274

Haywood, R. D., Collier Cameron, A., Queloz, D., et al. 2014, MNRAS, 443, 2517

Herrero, E., Lanza, A. F., Ribas, I., Jordi, C., & Morales, J. C. 2013, A&A, 553, A66

Herrero, E., Lanza, A. F., Ribas, I., et al. 2014, A&A, 563, A104

Huber, K. F., Czesla, S., Wolter, U., & Schmitt, J. H. M. M. 2010, A&A, 514, A39

Jetsu, L. 1996, A&A, 314, 153

Kallrath, J., & Milone, E. F. 1999, Eclipsing binary stars : modeling and analysis / Joseph Kallrath, Eugene F. Milone. New York : Springer, 1999. (Astronomy and astrophysics library)

Kolláth, Z., & Oláh, K. 2009, A&A, 501, 695

Kovari, Z., & Bartus, J. 1997, A&A, 323, 801

Kővári, Z., & Oláh, K. 2014, Space Sci. Rev., 186, 457

Lanza, A. F. 2014, in the 18th Cambridge Workshop on Cool Stars, Stellar Systems, and the Sun, Proceedings of Lowell Observatory, edited by G. van Belle & H. Harris; p. 811 [`http: arxiv.org/abs/1408.6049`]

Lanza, A. F., Catalano, S., Cutispoto, G., Pagano, I., & Rodono, M. 1998, A&A, 332, 541

Lanza, A. F., Rodonò, M., Pagano, I., Barge, P., & Llebaria, A. 2003, A&A, 403, 1135

Lanza, A. F., Rodonò, M., & Pagano, I. 2004, A&A, 425, 707

Lanza, A. F., Piluso, N., Rodonò, M., Messina, S., & Cutispoto, G. 2006, A&A, 455, 595

Lanza, A. F., Bonomo, A. S., & Rodonò, M. 2007, A&A, 464, 741

Lanza, A. F., Pagano, I., Leto, G., et al. 2009, A&A, 493, 193

Lanza, A. F., Aigrain, S., Messina, S., et al. 2009, A&A, 506, 255

Lanza, A. F., Bonomo, A. S., Moutou, C., et al. 2010, A&A, 520, A53

Lanza, A. F., Bonomo, A. S., Pagano, I., et al. 2011, A&A, 525, A14

Lanza, A. F., Das Chagas, M. L., & De Medeiros, J. R. 2014, A&A, 564, A50

Lehtinen, J., Jetsu, L., Hackman, T., Kajatkari, P., & Henry, G. W. 2011, A&A, 527, A136

Lindborg, M., Mantere, M. J., Olspert, N., et al. 2013, A&A, 559, A97

Lockwood, G. W., Skiff, B. A., Henry, G. W., et al. 2007, ApJS, 171, 260

McQuillan, A., Aigrain, S., & Mazeh, T. 2013, MNRAS, 432, 1203

McQuillan, A., Mazeh, T., & Aigrain, S. 2014, ApJS, 211, 24

Messina, S. 2008, A&A, 480, 495

Mosser, B., Baudin, F., Lanza, A. F., et al. 2009, A&A, 506, 245

Narayan, R., & Nityananda, R. 1986, ARA&A, 24, 127

Nutzman, P. A., Fabrycky, D. C., & Fortney, J. J. 2011, ApJ, 740, L10

Oshagh, M., Santos, N. C., Boisse, I., et al. 2013, A&A, 556, A19

Piskunov, N. E., Tuominen, I., & Vilhu, O. 1990, A&A, 230, 363

Poe, C. H., & Eaton, J. A. 1985, ApJ, 289, 644

Press, W. H., Teukolsky, S. A., Vetterling, W. T., & Flannery, B. P. 2002, Numerical recipes in C++ : the art of scientific computing by William H. Press. xxviii, 1,002 p. : ill. ; 26 cm. Includes bibliographical references and index. ISBN : 0521750334

Rauer, H., Catala, C., Aerts, C., et al. 2014, Experimental Astronomy, 38, 249

Reinhold, T., Reiners, A., & Basri, G. 2013, A&A, 560, A4

Rice, J. B., & Strassmeier, K. G. 2000, A&AS, 147, 151

Roettenbacher, R. M., Monnier, J. D., Harmon, R. O., Barclay, T., & Still, M. 2013, ApJ, 767, 60

Rodono, M., Cutispoto, G., Pazzani, V., et al. 1986, A&A, 165, 135

Rodonò, M., Cutispoto, G., Lanza, A. F., & Messina, S. 2001, Astronomische Nachrichten, 322, 333

Sanchis-Ojeda, R., & Winn, J. N. 2011, ApJ, 743, 61

Sanchis-Ojeda, R., Winn, J. N., & Fabrycky, D. C. 2013, Astronomische Nachrichten, 334, 180

Savanov, I. S., & Strassmeier, K. G. 2008, Astronomische Nachrichten, 329, 364

Savanov, I. S., & Strassmeier, K. G. 2005, A&A, 444, 931

Schneider, J. 2000, From Giant Planets to Cool Stars, ASP Conf. Series, C. A. Griffith and M. S. Marley (Eds.), vol. 212, p. 284

Silva, A. V. R. 2003, ApJ, 585, L147

Silva-Valio, A. 2008, ApJ, 683, L179

Silva-Valio, A., Lanza, A. F., Alonso, R., & Barge, P. 2010, A&A, 510, A25

Silva-Valio, A., & Lanza, A. F. 2011, A&A, 529, A36

Strassmeier, K. G. 2009, A&ARv, 17, 251

Strassmeier, K. G., & Bopp, B. W. 1992, A&A, 259, 183

Strassmeier, K. G., & Olah, K. 1992, A&A, 259, 595

Strassmeier, K. G., Bartus, J., Cutispoto, G., & Rodono, M. 1997, A&AS, 125, 11

Tikhonov, A. N., & Goncharsky, A. V. 1987, Ill-posed problems in the natural sciences, Moscow: MIR Publishers, 1987, 344 p., Advances in science and technology in the USSR. Mathematics and mechanics series

Titterington, D. M. 1985, A&A, 144, 381

Vogt, S. S., Penrod, G. D., & Hatzes, A. P. 1987, ApJ, 321, 496

Wolter, U., Schmitt, J. H. M. M., Huber, K. F., et al. 2009, A&A, 504, 561